distorted by the terrain-following velocity field. On the BTF grid, the tracer correctly returns to its original shape having cleared the mountain by $t = 10\,000\,\mathrm{s}$, but this is not the case with centred linear scheme on the cut cell grid. Here, the tracer has spread vertically due to increased numerical errors when the tracer is transported between layers. Dispersion errors are apparent with grid-scale oscillations that travel in the opposite direction to the wind (figure 3d) and some artifacts remain above the mountain peak.

A small improvement is obtained on the BTF grid by using the upwind-biased cubic scheme: as seen in figure 3e, errors are less than 0.02 in magnitude and errors are confined to the expected region of the tracer. However, results are substantially improved by using the upwind-biased cubic scheme on the cut cell grid (figure 3f). Results on the SLEVE grid are comparable to those on the cut cell grid except that the artifacts above the mountain peak with the centred linear scheme on the cut cell grid are not present on the SLEVE grid (not shown).

ℓ_2 errors and tracer extrema for this test are compared with the horizontal advection results in table 1. In the terrain following velocity field, tracer accuracy is greatest on the BTF grid. Errors are about ten times larger on the SLEVE and cut cell grids compared to the BTF grid.

We conclude from this test that accuracy depends upon alignment of the flow with the grid, and accuracy is not significantly reduced by grid distortions. Error on the BTF grid in the terrain following advection test is comparable with the error on the SLEVE grid in the horizontal advection test.

c. Stratified atmosphere initially at rest

An idealised terrain profile is defined along with a stably stratified atmosphere at rest in hydrostatic balance. The analytic solution is time-invariant, but numerical errors in calculating the horizontal pressure gradient can give rise to spurious velocities which become more severe over steeper terrain (Klemp 2011).

The test setup follows the specification by Klemp (2011). The domain is 200 km wide and 20 km high, and the grid resolution is $\Delta x = \Delta z^{\star} = 500\,\mathrm{m}$. All boundary conditions are no normal flow.

The wave-shaped mountain profile has a surface height, h, given by

$$h(x) = h_0 \exp\left(-\left(\frac{x}{a}\right)^2\right)\cos^2(\alpha x) \tag{20}$$

where $a = 5\,\mathrm{km}$ is the mountain half-width, $h_0 = 1\,\mathrm{km}$ is the maximum mountain height and $\lambda = 4\,\mathrm{km}$ is the wavelength. For the optimised SLEVE grid, the large-scale component h_1 is specified as

$$h_1(x) = \frac{1}{2} h_0 \exp\left(-\left(\frac{x}{a}\right)^2\right) \tag{21}$$

and, following Leuenberger et al. (2010), $s_1 = 4\,\mathrm{km}$ is the large scale height, $s_2 = 1\,\mathrm{km}$ is the small scale height, and the optimal exponent value of $n = 1.35$ is used.

Tests were performed with two different stability profiles, both having an initial potential temperature field with $\theta(z=0) = 288\,\mathrm{K}$ and a constant static stability with Brunt-Väisälä frequency $N = 0.01\,\mathrm{s}^{-1}$ everywhere, except for a more stable layer of $N = 0.02\,\mathrm{s}^{-1}$. Figure 4a shows where this inversion layer is positioned in the two tests: the 'high inversion' test follows Klemp (2011), placing the layer between $2\,\mathrm{km} \leq z \leq 3\,\mathrm{km}$; the 'low inversion' test is designed to challenge the numerics on the cut cell grid by placing the inversion layer between $0.5\,\mathrm{km} \leq z \leq 1.5\,\mathrm{km}$ so that it intersects the terrain.

The Exner function of pressure is calculated so that it is in discrete hydrostatic balance in the vertical direction (Weller and Shahrokhi 2014). The damping function, μ, is set to $0\,\mathrm{s}^{-1}$. Unlike Klemp (2011), there is no eddy diffusion in the equation set.

The tests were integrated forward by 5 hours using a timestep $\Delta t = 100\,\mathrm{s}$ on the BTF, SLEVE and cut cell grids, and a regular grid with flat terrain. The results presented in figure 4b, which use

There is too much in this sentence

a curl-free pressure gradient, have maximum spurious values of w of $0.37\,\mathrm{m\,s^{-1}}$ on the BTF grid with the high inversion layer, compared with a maximum of $\sim 7\,\mathrm{m\,s^{-1}}$ found by Klemp (2011) using their improved horizontal pressure gradient formulation. Unlike the result from Klemp (2011), the SLEVE grid does not significantly reduce vertical velocities compared to the BTF grid. For the high inversion test, errors are two orders of magnitude smaller on the cut cell grid with vertical velocities of $\sim 1 \times 10^{-4}\,\mathrm{m\,s^{-1}}$, but this advantage is lost when the inversion layer is lowered to intersect the terrain. ~~The smallest error of $\sim 1 \times 10^{-10}\,\mathrm{m\,s^{-1}}$ is found on the regular grid.~~ The results for the high inversion test in figure 4b have maximum errors that are comparable with Weller and Shahrokhi (2014) but, due to the more stable split into implicitly and explicitly treated terms (described in the appendix), the errors decay over time due to the dissipative nature of the advection scheme.

Good et al. (2014) found the maximum vertical velocity in their cut cell model was $1 \times 10^{-12}\,\mathrm{m\,s^{-1}}$, which is better than any result obtained here. It is worth noting that our model stores values at the geometric centre of cut cells, whereas the model used by Good et al. (2014) has cell centres at the centre of the uncut cell, resulting in the centre of some cut cells being below the ground (S.-J. Lock 2014, personal communication). This means that the grid is effectively regular when calculating horizontal and vertical gradients. This would account for the very small velocities found by Good et al. (2014).

In summary, spurious velocities in the resting atmosphere test were similar on terrain following and cut cell grids, with lower errors compared to those from Klemp (2011). TODO: *we previously concluded, "The maximum vertical velocity was significantly decreased on the cut cell grid, so we conclude that non-orthogonality, or lack of alignment of the grid with surfaces of constant*

This is a terrific new result. Representing a stably stratified atmosphere is a key reason why people say that cut cells a *gravitational potential are a significant cause of numerical error in this test." — but what can we say now we have the high/low inversion tests?*

d. Gravity waves

The test originally specified by Schär et al. (2002) prescribes flow over terrain with small-scale and large-scale undulations which induces propagating and evanescent gravity waves.

Following Melvin et al. (2010), the domain is 300 km wide and 30 km high. The mountain profile has the same form as equation (20), but the gravity waves tests have a mountain height of $h_0 = 250\,\mathrm{m}$. As in the resting atmosphere test, $a = 5\,\mathrm{km}$ is the mountain half-width and $\lambda = 4\,\mathrm{km}$ is the wavelength.

A uniform horizontal wind $(u, w) = (10, 0)\,\mathrm{m\,s^{-1}}$ is prescribed in the interior domain and at the inlet boundary. No normal flow is imposed at the top and bottom boundaries and the velocity field has a zero gradient outlet boundary condition.

The initial thermodynamic conditions have constant static stability with $N = 0.01\,\mathrm{s^{-1}}$ everywhere, such that

$$\theta(z) = \theta_0 \exp\left(\frac{N^2}{g} z\right) \tag{22}$$

where the temperature at $z = 0$ is $\theta_0 = 288\,\mathrm{K}$. Potential temperature values are prescribed at the inlet and upper boundary using equation (22), and a zero gradient boundary condition is applied at the outlet. At the ground, fixed gradients are imposed by calculating the component of $\nabla\theta$ normal to each face using the vertical derivative of equation (22). For the Exner function of pressure, hydrostatic balance is prescribed on top and bottom boundaries and the inlet and outlet are zero normal gradient.

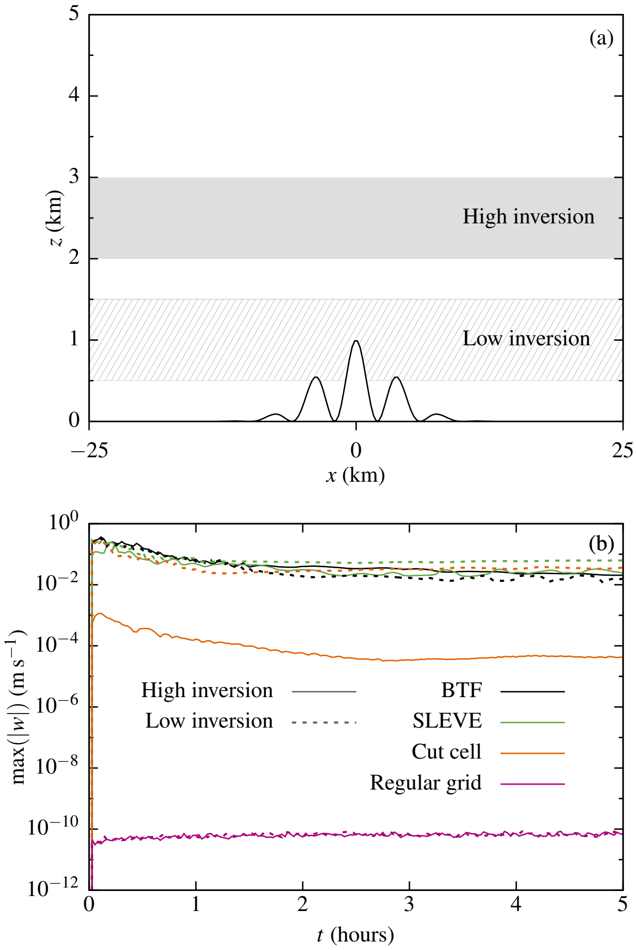

FIG. 4. Setup and results of a stratified atmosphere initially at rest. Tests are performed on four grids for two different stability profiles, with panel (a) showing the placement of the inversion layer in the two profiles. The low inversion is positioned so that it intersects the terrain, shown immediately above the x axis. In each test, the inversion layer has a Brunt-Väisälä frequency $N = 0.02\,\mathrm{s}^{-1}$ and $N = 0.01\,\mathrm{s}^{-1}$ elsewhere. Panel (b) shows the maximum magnitude of spurious vertical velocity, w ($\mathrm{m\,s}^{-1}$), with results on BTF, SLEVE, cut cell and regular grids using the model from Weller and Shahrokhi (2014) which includes a curl-free pressure gradient formulation. Results for the high inversion test are shown with solid lines, the low inversion test with dashed lines.